ADVANCED FUNCTIONAL MATERIALS
www.afm-journal.de

Inkjet Printed Metal–Organic Frameworks for Non-Volatile Memory Devices Suitable for Printed RRAM

*Yan Liu, Franz Fischer, Hongrong Hu, Hartmut Gliemann, Carsten Natzeck, Matthias Schwotzer, Christian Rainer, Uli Lemmer, Christof Wöll, Ben Breitung, and Jasmin Aghassi-Hagmann**

Inkjet printing has emerged as a promising technique for patterning functional materials, offering significant advantages over traditional subtractive thin-film methods. Its versatility enables the structuring of various materials, expanding application ranges and minimizing waste through additive manufacturing. However, the limited availability of functional material-based inks suitable for inkjet printing presents challenges in ink formulation. HKUST-1, a 3D cubic metal–organic frameworks (MOFs) comprised of copper(II) ions coordinated to benzene-1,3,5-tricarboxylate (BTC) organic linkers, known for its porosity and tunability, have potential to enhance inkjet-printed devices. This study combines inkjet printing and evaporation-induced crystallization to structure HKUST-1, marking the first demonstration of nanocrystalline HKUST-1 integrated into a printed electronic device, specifically a memristor, where the MOF is prepared by inkjet printing of a precursor solution. Memristors, which change their resistance based on the external stimuli history, enabling the construction of resistive random-access memory (RRAM). The fabricated memristors in this study exhibit notable properties: low forming voltage, an R_{off}/R_{on} ratio of 10^4, a retention time of 600 s, and endurance exceeding 60 write and erase cycles. This research highlights the potential of integrating MOFs into inkjet printing, unlocking broader application possibilities, and advancing additive manufacturing for functional materials.

1. Introduction

Inkjet printing has gained significant recognition as a highly promising technique for patterning functional materials with various potential applications. Unlike subtractive thin film methods such as lithography, inkjet printing offers numerous advantages. It provides a broader selection of materials, expanding the range of applications, and embraces an additive manufacturing approach, effectively minimizing waste production, especially for large-scale device structuring.[1–3] Inkjet printing enables precise deposition of small ink volumes, offering high-resolution patterning. This precision is essential for the controlled fabrication of thin films with fine structures, which would be difficult to achieve with techniques such as screen printing or gravure printing.[4,5] Additionally, inkjet printing is a non-contact, additive manufacturing process. It offers significant flexibility in adjusting parameters such as drop size and drop spacing, which makes it easy to customize the printing process for different substrates and desired layer properties. Techniques like offset lithography and screen printing, due to their reliance on mechanical or physical templates, are less adaptable for such fine-tuning.[4,6] Moreover, inkjet printing allows wide range of ink property, while electric conductivity of solvents is critical for electrohydrodynamic atomization (EHDA).[7] It is also compatible with a wide range of substrates, including flexible materials, without requiring for pre- or post-processing steps as seen

Y. Liu, F. Fischer, H. Hu, B. Breitung, J. Aghassi-Hagmann
Institute of Nanotechnology (INT)
Karlsruhe Institute of Technology (KIT)
Kaiserstraße 12, 76131 Karlsruhe, Germany
E-mail: jasmin.aghassi@kit.edu

The ORCID identification number(s) for the author(s) of this article can be found under https://doi.org/10.1002/adfm.202412372

DOI: 10.1002/adfm.202412372

H. Gliemann, C. Natzeck, M. Schwotzer, C. Wöll
Institute of Functional Interfaces (IFG)
Karlsruhe Institute of Technology (KIT)
Kaiserstraße 12, 76131 Karlsruhe, Germany
C. Rainer, U. Lemmer
Light Technology Institute (LTI)
Karlsruhe Institute of Technology (KIT)
Kaiserstraße 12, 76131 Karlsruhe, Germany
C. Rainer, U. Lemmer
InnovationLab
Speyererstraße 4, 69115 Heidelberg, Germany
U. Lemmer
Institute of Microstructure Technology (IMT)
Karlsruhe Institute of Technology (KIT)
Kaiserstraße 12, 76131 Karlsruhe, Germany

in offset lithography or flexographic printing.[6,8] Though inkjet printing may exhibit lower resolution and crystal structure ordering compared to sputtering and lithography, its unique strengths compensate for these limitations. The versatility of inkjet printing allows the structuring of (nano)particulate or precursor-based (liquid) inks, greatly extending the range of patternable materials, including metals, ceramics, and polymers. This exceptional adaptability enhances the potential for creating complex structures and functional devices.[9,10]

Despite the evident potential of inkjet printing, the current availability of functional material-based inks suitable for this process remains limited. Formulating inks for specific materials presents challenges in achieving optimal viscosity, accommodating low-temperature processing for flexible substrates, and addressing other complexities. To realize the full potential of inkjet printing, the development of ink formulations and techniques to accommodate complex material classes is of utmost importance.

One such complex material class with tremendous potential for enhancing inkjet printed devices is metal-organic frameworks (MOFs). MOFs consist of metal ions connected by organic linkers, resulting in intricate structures with well-defined porosities.[11,12] MOF-based materials find applications in gas storage and separation,[13,14] catalysis,[15–17] sensing,[18,19] energy storage,[20] and memristors.[21] Traditionally, MOFs have been structured using subtractive photolithography and additive deposition methods, which involve complex procedures performed under high vacuum conditions.[22,23] In another approach MOFs were grown site-selectively by using top-down techniques such as microcontact printing and scanning probe-based nanografting methods to pattern self-assembled monolayers, followed by a bottom-up layer-by-layer (LBL) deposition of the MOF material on the activated surface areas. Although this approach results in well-defined micro and nano structures, the chemical incompatibility of substrates with the LBL process particularly in the case of polymers is a drawback, limiting or even avoiding this approach.[24,25] Integrating MOFs into additive manufacturing methods like inkjet printing would revolutionize their applicability and enable large-scale production of patterned MOF devices.[26] Only few inkjet printable MOF inks have been explored in the past, including precursor-based[27] and nanoparticulate inks.[28]

In our work, we introduce an ink system for $Cu_3(BTC)_2$ (BTC: 1,3,5-benzenetricarboxylate), also known as HKUST-1, a precursor-based ink developed by Zhuang et al.[27] This ink offers good printability when compared to other precursor-based inks while maintaining stability during the printing process. Furthermore, it enables room-temperature printing, enhancing the compatibility with various printed materials as well as the substrates. The ink operates on the principle of evaporation induced crystallization. A reliable method combining inkjet printing and evaporation-induced crystallization is employed for the construction of HKUST-1.[27,29] Notably, this is the first demonstration of inkjet-printed nanocrystalline HKUST-1 directly integrated into a printed electronic device, specifically a resistive random-access memory (RRAM) device also known as "memristor". This achievement bridges the gap between printed MOFs and their potential application in the field of printed electronics.

Here, the printed HKUST-1 was applied as the active layer of a memristor, an electronic device that can be conceptualized as a resistor with memory. A memristor is a two-terminal device that is able to alter its resistance based on the previous voltage applied to it, retaining this information over a specific period of time even when the power is turned off. This distinguishing feature sets the memristor apart from conventional passive circuit elements like resistors or capacitors, making it highly promising for applications such as non-volatile memory, neuromorphic computing, hardware security, and radio-frequency communications neural networking, and the potential revolution of brain-inspired computing systems and advanced artificial intelligence architectures.[30–32] Continued research and technological advancements are expected to unlock the full capabilities of memristors, enabling their integration into diverse electronic systems and facilitating the emergence of novel functionalities. The memristors fabricated in this study exhibit promising properties, including an R_{off}/R_{on} ratio of 10^4, a retention time of 600 s, and endurance of over 60 write and erase cycles. Notably, these MOF based memristors show a greatly decreased forming voltage, around1 V, which appears to be in the range of operation voltage.[33]

In summary, integrating inkjet-printed MOFs into memristors represents a significant milestone, expanding their potential applications and paving the way for the widespread production of patterned MOF devices. This development unlocks the full capabilities of MOFs and contributes to advancements in additive manufacturing techniques for functional materials, elevating the position of inkjet printing in the field of structuring methods.

2. Results and Discussion

This work reports on a memristor, produced by a combination of inkjet printing and evaporation-induced crystallization of the active material, i.e., HKUST-1 (MOF).[27,29] The memristor was fabricated by a sequence of different production steps as illustrated in **Figure 1**.

First, the bottom indium tin oxide (ITO) electrode was patterned through laser ablation of an ITO-coated glass substrate, followed by O_2 plasma surface treatment for both cleaning purposes and to enhance surface hydrophilicity (Figure 1a–c). Next, the prepared HKUST-1 ink was deposited onto the ITO electrode using inkjet printing. It is noteworthy that the HKUST-1 ink serves as the precursor for the growth of HKUST-1 crystals (Figure 1d). Subsequently, the substrate was placed in a desiccator containing a vial of methanol (Figure 1e). The desiccator's internal pressure was reduced to 30 mbar and maintained for 20 min to facilitate methanol evaporation. The nucleation and growth of HKUST-1 crystallites was triggered by the methanol vapor, which also lead to a sufficiently slow crystallization process, resulting in the formation of a uniform HKUST-1 film.[29] To obtain a densely packed HKUST-1 layer and to adjust the layer thickness, the steps depicted in Figure 1d,e were repeated multiple times. Afterward, the sample was rinsed with methanol, dried, and subjected to overnight vacuum storage. Subsequently, the silver top electrode was patterned using inkjet printing, followed by annealing at 100 °C for 1 h for sintering (Figure 1f,g). The scheme in Figure 1h shows the final layer structure of the memristor.

Achieving refined printed patterns and fabricating reliable memristor devices with inkjet-printing requires developing

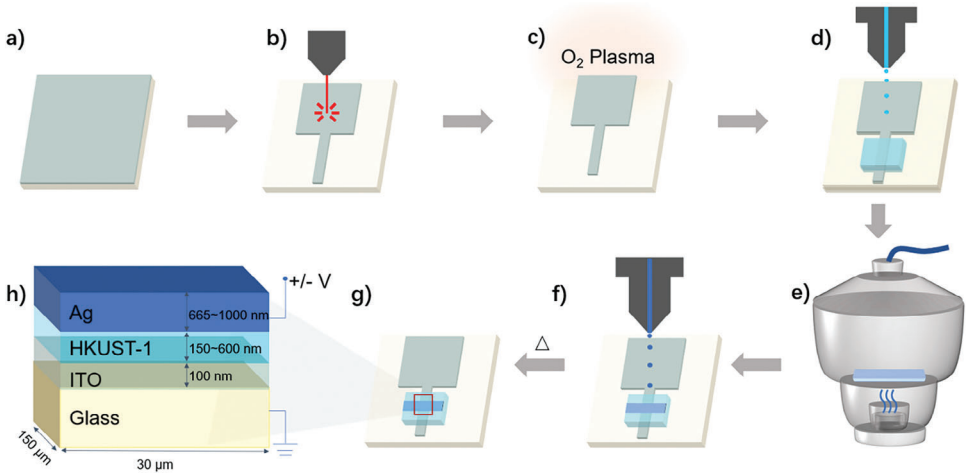

Figure 1. Fabrication of the printed HKUST-1 memristor. a) ITO coated glass as substrate. b) The ITO layer is pattern using laser ablation. c) O_2 plasma treatment for surface cleaning and to induce increased hydrophilicity. d) Inkjet printing of the HKUST-1 precursor solution (HKUST-1 ink). e) Vapor induced crystallization of HKUST-1. f) Inkjet printing of the Ag top electrode after cleaning. g) After sintering at 100 °C for 1 h, the memristor as shown in (h) is completed.

stable inks with appropriate rheological properties. The jetting behavior of the ink can be evaluated using the Ohnesorge number (Oh, reciprocal of Fromm number Z), which is defined by the equation:

$$\mathrm{Oh} = \frac{\sqrt{\mathrm{We}}}{Re} = \frac{\eta}{\sqrt{\gamma \rho \alpha}} \quad (1)$$

where η, γ, and ρ represent the ink's viscosity (cp), surface tension (mN m^{-1}) (Figure S1, Supporting Information), and density (g cm^{-3}), respectively, while α denotes the diameter (µm) of the jetting nozzle.[34] If the Fromm value Z falls within the range of 1 to 10 ($1 < Z < 10$), the ink composition is expected to form stable droplets for inkjet printing.[35–37] The Fromm number of HKUST-1 ink is 6.3577, demonstrating that the HKUST-1 ink jets stably and is well-suited for the inkjet printing system. Detailed rheological parameters of the HKUST-1 ink are provided in the supporting information (Table S1, Supporting Information). Moreover, key inkjet printing parameters, such as waveform, voltage, and drop spacing, were optimized for consistent droplet formation and precise HKUST-1 layer deposition. The selected waveform prevented satellite droplets, ensuring uniform layering (see Figure S2, Supporting Information).

X-ray diffraction (XRD) characterization provides valuable insights into the crystal structure and phase composition of the inkjet-printed HKUST-1 layer, confirming its integrity and suitability for further analysis and potential applications. Therefore, an inkjet-printed HKUST-1 film comprising three printed layers (repeated three times in steps d and e in Figure 1) was prepared and characterized using XRD to examine the crystal structure. **Figure** 2a illustrates the XRD pattern of the HKUST-1 film before and after annealing, along with the calculated pattern for comparison (ICSD# 130295). The XRD pattern clearly exhibits all the expected reflections corresponding to HKUST-1, with no additional reflections present. This observation indicates the desired phase purity of the HKUST-1 structure (Figure 2b). Moreover, the XRD pattern does not demonstrate any discernible preferred orientation. This suggests the presence of polycrystalline HKUST-1 with relatively small crystallite sizes due to the broadened peaks.

Figure 2c presents the Fourier-transform infrared (FT-IR) spectrum of the printed HKUST-1 layer, providing evidence of the nearly complete transformation of the BTC precursor with Cu^{2+} during the methanol-induced crystallization process, leading to the formation of HKUST-1. A prominent feature in the spectrum is the significant reduction in intensity of the C═O double bond peak at 1720 cm^{-1}, which corresponds to unreacted BTC precursor. This reduction indicates the conversion of the C═O double bond into a C-O single bond upon the formation of HKUST-1. Furthermore, the emergence of the Cu-O bond peak at 750 cm^{-1} is the direct result of this cleavage. Additionally, distinctive vibration modes associated with the former carboxylic group of BTC, now bonded to Cu, are observed at 1646, 1448, and 1371 cm^{-1}. These modes correspond to the asymmetric stretching and symmetric stretching of the carboxylic group, respectively. The FTIR analysis provides compelling evidence for the structural transformations that occur during the inkjet printing and crystallization processes, confirming the successful formation of HKUST-1 and the chemical changes involved in the conversion of the BTC precursor.

In order to gain deeper insights into the layered structure of the memristor, a focused ion beam (FIB) technique was employed to precisely cut the sample for cross-section scanning electron microscopy (SEM) analysis. **Figure** 3a,b provides a visual representation of the sandwich-like configuration observed within the memristor. The structure comprises a glass substrate as the foundation, followed by the ITO electrode, the HKUST-1 layer, and the printed Ag-electrode situated atop. Notably, the Ag-electrode is composed of a nanoparticulate ink material. To investigate the surface roughness and morphology, atomic force microscopy (AFM) was employed to analyze the topography of the printed HKUST-1 layer. The resulting AFM data were evaluated using Gwyddion.[38] As depicted in Figure 3c, a selected

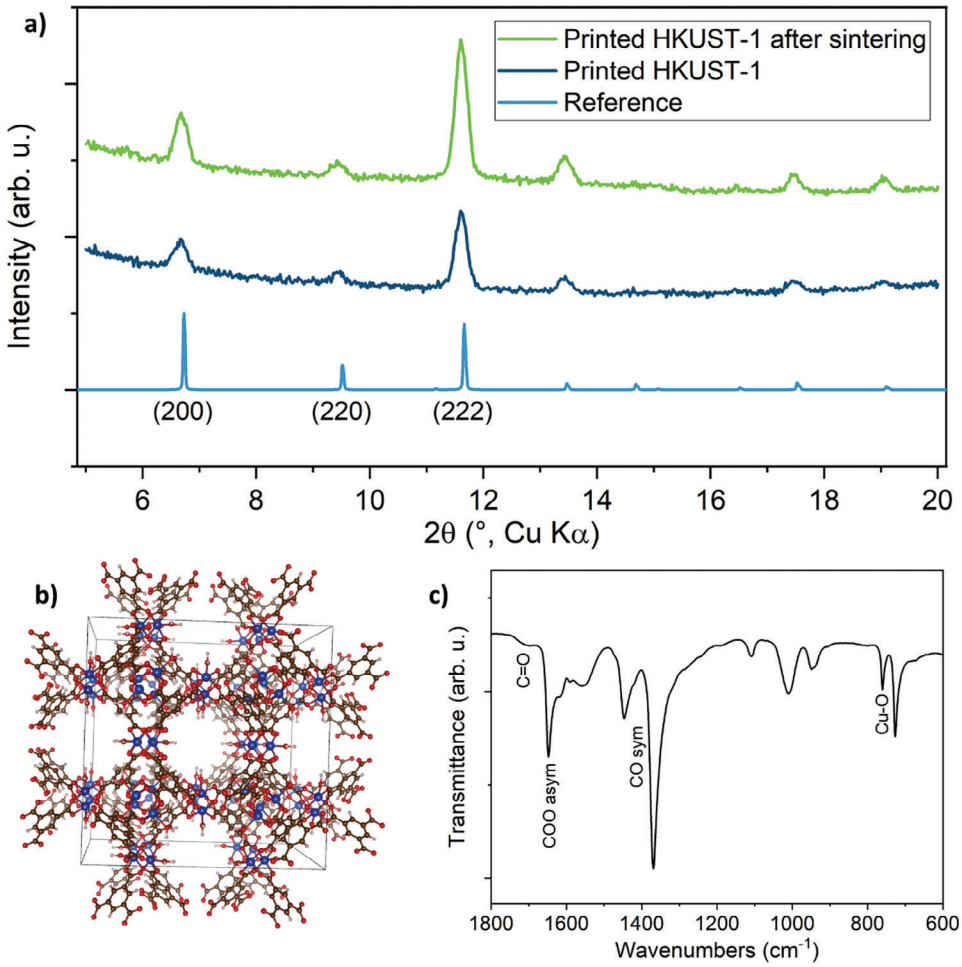

Figure 2. a) XRD pattern of the inkjet-printed HKUST-1 layer before and after annealing. A reference pattern of HKUST-1 is shown in the bottom part (ICSD# 130295). b) crystal structure of HKUST-1. The color code is: blue = Cu, red = O, brown = C, white = H. c) FT-IR spectra of the inkjet-printed HKUST-1 layer.

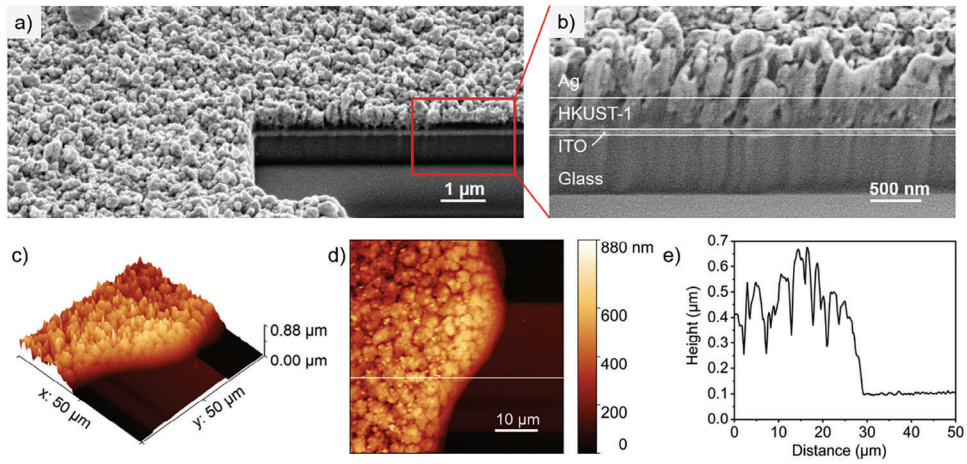

Figure 3. a) SEM micrograph of the printed HKUST-1 layer. FIB cutting was employed to elucidate the layered structure. b) visual representation of the layered structure. c) AFM measurement of the border area of the printed HKUST-1. d) Top view of the same area as in (c). e) Line scan along the white line indicated in (d).

area of around 2500 μm^2 at the periphery of the printed HKUST-1 layer is shown. Beneath the rough HKUST-1 layer, the presence of the ITO electrode is discernible, indicating complete coverage at the termination point of the electrode section. A top-view heatmap, representing the material's height, provides insights into the printed HKUST-1 sheet's maximum height, which ranges from 600 to 880 nm (Figure 3d). This observation aligns with the XRD results, which indicate a nanocrystalline structure rather than a well-ordered region characterized by large crystallites. Furthermore, a line scan along the indicated white line in Figure 3d was conducted (Figure 3e), revealing two distinct layers within the structure. The bottom layer, which corresponds to ITO layer, has a measured thickness of approximately 100 nm. Above this, the HKUST-1 layer, exhibits significant surface roughness with height variations ranging from 250 to 700 nm (the thickness ranges from 150 to 600 nm), with a foundational height thickness of ≈150 nm for the dense sheet structure.

The conducted measurements provide compelling evidence of an inkjet-printed memristor characterized by well-defined layer geometry. The active layer consists of nanocrystalline HKUST-1, while the bottom and top electrodes comprise ITO and printed Ag, respectively. The use of complementary techniques, such as XRD and IR spectroscopy, verifies the presence of nanocrystalline HKUST-1 with the desired crystal structure. Moreover, these analyses indicate only minimal traces of unreacted linker material. For additional characterization of the ITO substrates and HKUST-1 layer, including contact angle measurements, AFM and SEM analysis is displayed in Figures S3–S5 (Supporting Information).

After confirming the precise layered structure of the memristor, electrical characterizations were conducted to evaluate its performance. The HKUST-1 memristor presented here belongs to a non-volatile type that can switch between two distinct resistive states: a high resistive state (HRS) and a low resistive state (LRS). This digital switching behavior is characterized by the transition between these two resistance states. To study this switching behavior, a current-voltage (*I–V*) analysis was performed under ambient conditions, where a bias voltage was applied to the top electrode (printed Ag) while the bottom electrode remained grounded. The voltage was swept between two limiting values, and the resulting current flow was measured (0 V → 2 V → 0 V → -3 V → 0 V). Depending on the resistive state of the memristor, the current can be low or high, with a steep increase or decrease observed during the transition between states.

Typically, for such digital memristors, an initial sweeping cycle known as the formation cycle is necessary. This cycle involves sweeping the voltage toward a higher potential, leading to the formation of a substructure within the memristor as explained later. **Figure** 4a illustrates five representative sweeping cycles in the positive voltage range, including the forming voltage. During the forming cycle (the 1st cycle in Figure 4a), the voltage was swept from 0 to 2 V at a rate of 0.02 V/step, and an abrupt increase in current at around1 V indicated the formation of the LRS. The LRS still maintained when the voltage was swept back from +2 V to 0 V at a rate of 0.02 V/step. The subsequent set processes, which means to switch the device from HRS to LRS in a new resistive switching cycle, followed the same voltage sweeping protocol and were triggered at the voltage of ca. 1 V. The forming voltage falls within the range of set voltages, implying a huge advantage for circuit level application since the redundant forming process will be eliminated. A compliance current (CC) of 0.5 mA was introduced to limit the current and prevent device breakdown, and it was reached during this steep increase. Sweeping measurements under different CC were also investigated. For details, please refer to Figure S6 (Supporting Information).

Then, the voltage was swept from 0 to −3 V at rate of 0.03 V/step in the absence of a CC, and then back to 0 V. During the first negative sweep, the memristor was switched from the LRS to the HRS, a process known as the reset process. Subsequently, the potential is swept upward, initiating a new cycle. As the set and reset processes depend on the polarity of the voltage, the HKUST-1 memristor can be classified as a bipolar device.

The voltage sweeping measurements conducted demonstrate the ability of the memristor to adapt an HRS and an LRS by modulating the applied potential. The evaluation of a memristor's quality often relies on the resistance disparity between these two states. Therefore, Figure 4c presents a comparison of the resistance of the HRS and LRS over a cycling period of more than 60 cycles. To be able to compare the resistances of the LRS and the HRS at different cycles, the resistance was measured at 0.01 V each cycle. With a few exceptions, Figure 4c unequivocally illustrates the existence of two distinct resistive states with a resistance difference of approximately 10^4 commonly referred to as the R_{off}/R_{on} ratio. While the HRS exhibits a greater dispersion in resistance values across the cycles, a discernible discrepancy is still evident.

To further assess the longevity of information storage within the HKUST-1 memristor, retention measurements were performed to evaluate the stability of the resistive states over time. Figure 4d demonstrates that the R_{off}/R_{on} ratio of 10^4 can be maintained for nearly 600 s, after which the LRS gradually increases the resistance, resulting in a decrease in the R_{off}/R_{on} ratio to 10^3. The observed increase in LRS value around 600 s is primarily due to the diffusion and degradation of conductive paths within the memristive device. This leads to a rise in resistance and a consequent decrease in the R_{off}/R_{on} ratio.

The observed electrical characteristics of the memristor stem from the combined properties of the constituent materials within the memristor stack, namely the active HKUST-1 material, the printed Ag top electrode, and the laser-ablated ITO bottom electrode. It is important to note that the memristor presented in this study differs from thin-film memristors commonly prepared using thin film techniques, which typically exhibit film qualities and thicknesses in the range of several nanometers rather than several hundreds of nanometers as demonstrated here. This distinction in properties is inherent to the manufacturing approach employed. The advantage of the presented system lies in its ease of production and the simplicity of the additive manufacturing technique used, which eliminates the need for vacuum-based processes such as sputtering or e-beam techniques. Furthermore, this approach enables the utilization of complex materials classes like MOFs, thereby paving the way for the integration of such promising materials in printed electronics. While the reversibility of the presented memristor may not be on par with state-of-the-art thin-film memristors, the primary focus is on establishing an alternative means of producing memristors and

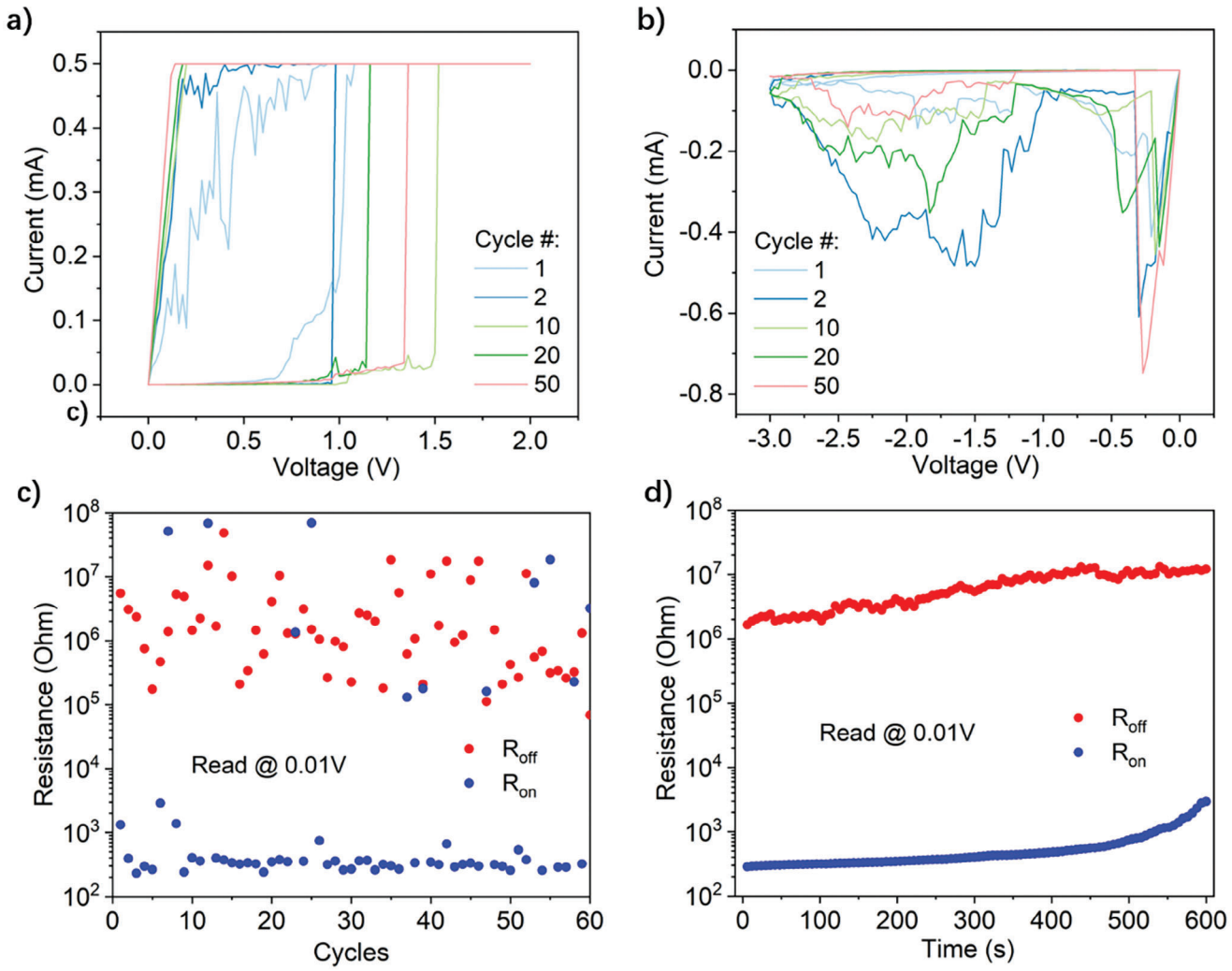

Figure 4. a) *I–V* curves depicting the electroforming voltage sweep (the 1st) within the positive voltage range, alongside the representative set processes (the 2nd, the 10th, the 20th, and the 50th). Notably, the LRS is achieved utilizing a set CC of 0.5 mA. b) *I–V* curves illustrating the representative reset processes conducted within the negative voltage range, resulting in the establishment of the HRS. c) Performance assessment of the inkjet-printed memristor's endurance during the initial 60 cycles, while operating under a voltage sweeping mode. d) Assessment of device retention in both the HRS and LRS.

exploring new areas of application, rather than competing with conventional manufacturing techniques.

In thin-film memristors, the switching mechanism of a digital memristor is often described as follows (refer to **Figure 5**). The system comprises an "inert" and an "active" electrode, separated by the active material. In the system discussed in this work, the Ag electrode serves as the active electrode, while the ITO electrode acts as the inert electrode. Initially, a forming process is required, which occurs while a positive voltage is applied to the active electrode. During this forming process, Ag is oxidized to Ag+, which diffuses through the active material along the applied electrical field and is reduced on the counter electrode. This electrodeposition phenomenon leads to the formation and growth of one or more conducting Ag filaments, which eventually make contact with both electrodes, resulting in the LRS of the memristor.[39–45] Subsequent cycles involve the dismantling and reformation of these conducting filaments, allowing for the switching of resistive states based on the previously applied potentials.

For the printed memristors, we postulate that this process is analogous, albeit influenced by the electrode distances and the distinctive morphology of HKUST-1 with its inherent features. HKUST-1 crystals consist of Cu paddlewheel clusters connected by BTC linkers. The structure features three distinct cavities: a small octahedral cage with a 4.1 Å window and two larger cuboctahedral cages interconnected by a 6.9 Å window (Figures 2b and 5).[39–41] The diameter of an Ag^+ ion is approximately 2.3 Å,[38] which is smaller than the size of the windows and the cavities in HKUST-1. The polycrystalline nature of HKUST-1, in particular its grain boundaries and highly porous structure, may allow Ag^+ ions to diffuse into or through the layer. The contact with the counter electrode can reduce Ag^+ to Ag, which leads to the formation of tiny filaments that penetrate the HKUST-1 structure and the formation of conductive pathways within the

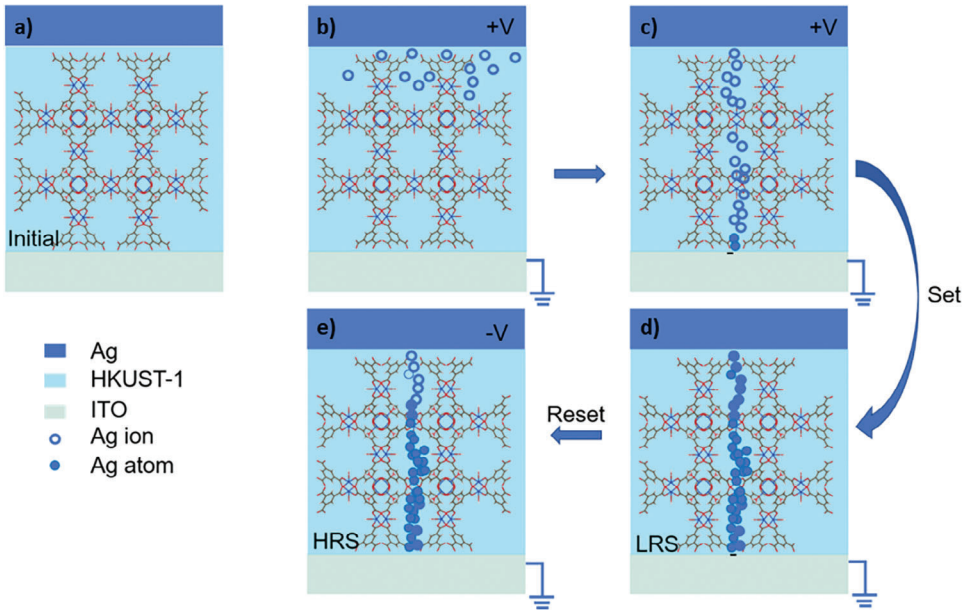

Figure 5. a) Initial state of the inkjet-printed memristor as prepared. b) Evolution during the positive voltage sweep (set): Silver cations (Ag^+) are generated and subsequently migrate toward the opposing electrode. c) Reduction of Ag^+ ions takes place. d) Formation of a dendritic structure bridging both electrodes, leading to the establishment of the LRS in the memristor. e) During the reset process, dismantling of the dendritic structure occurs, resulting in the HRS of the memristor.

printed HKUST-1 layer, which in turn impact the performance of the memristor.[27] For most materials, the thickness of the active layer mainly affects the forming voltage required for initial resistive switching, with thicker layers needing higher voltages.[33,46] Subsequent switching (set/reset), we believe, is more dependent on the porosity of the active layer and electrode material compared to the thickness, particularly when using porous materials like HKUST-1. This characteristic also offers opportunities for fine-tuning the electrical performance of the memristor, such as adjusting porosity or particle size. However, these structural complexities also present challenges. For instance, the relatively short retention times of the LRS can be attributed to the need for long Ag filaments, resulting in a larger surface area, thereby increasing the likelihood of Ag filament atom/ion diffusion and filament breakage. To prove that the Ag electrode plays a decisive role in the memristive behavior, a comparison experiment was conducted by fabricating an Au/HKUST-1/Au device, which exhibited no resistive switching behavior. For further details, please refer to Figure S7 (Supporting Information).

In order to gain insights into the contribution of different material states to the HRS and LRS, as well as to postulate a conduction mechanism, an analysis of the I-V curve was conducted. A well-known theory for the development of the LRS and HRS is the assumption that a conducting filament will grow over memristor operation between the electrodes.[39–42] To support the theory of such a filament based resistive switching mechanism of the printed HKUST-1 memristor, we analyzed the *I–V* curves during the appearance of the LRS and HRS state, respectively. **Figure 6** illustrates the set process (positive voltage portion of Figure 4a) on a double logarithmic scale, which involves a transition from HRS (the lower curve) to LRS (the upper curve). To better understand the conduction mechanism, a linear fit was applied to the curves to extract the slopes, which were compared with ohmic conduction and space charge limited conduction (SCLC) theory to infer the underlying or dominant mechanisms during operation.[47] We identify distinct regions in the *I–V* curve where the slope changes. Different slope from different regions typically correspond to the theoretical model of different conduction mechanisms. The conduction of SCLC consists of three parts: the ohmic region, the SCLC with unfilled traps (Child's law), and SCLC with filled traps (the steep increase in the high field region).

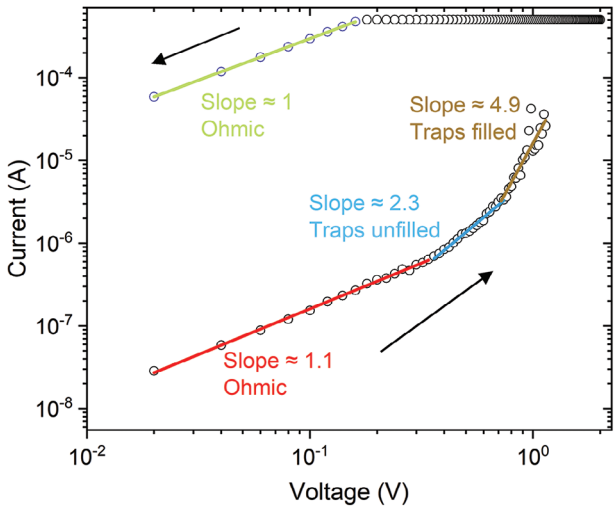

Figure 6. Double-logarithmic I-V curve for regions with different conducting mechanisms, including ohmic conduction and SCLC theory.

For ohmic conduction, the slope of the log I-log V curve may be calculated using as 1 according to Equation (2):

$$J_{Ohmic} \propto E \quad (2)$$

For the SCLC with unfilled traps slope of the log I-log V curve may be calculated as 2 according to Equation (3):

$$J_{Trap-unfilled\ SCLC} \propto E^2 \quad (3)$$

For the SCLC with filled traps, the slope of the log I-log V curve can be calculated using the Equation (4) and is expected to be >2:

$$J_{Trap-filled\ SCLC} \propto E^n, n > 2 \quad (4)$$

Different slopes can be observed in the low-voltage and high-voltage regions of the *I–V* curve. Starting at low voltages and in the HRS state the initial phase of the process, represented with the red line, exhibits an ohmic behavior. The slope of this fit is 1.1, indicating a small current due to the limited presence of thermally excited charge carriers in the active HKUST-1 layer. As the applied voltage increases, according to the SCLC theory, electrons from the electrodes can be injected into the MOF layer, partially filling traps and leading to a gradual increase in conductance.[48,49] This corresponds to a steeper slope in the *I–V* curve, classified as trap-unfilled SCLC. With further voltage increase, the SCLC theory suggests that electrons from the electrodes fill the traps in the active layer, leading to an exponential growth in current. This signifies a transition from trap-unfilled to trap-filled SCLC (slope changes from 2.3 to 4.9). For slopes >2, the SCLC model assumes traps distributed in energy, decreasing with distance from the conduction band. A high density and distribution of trap states is likely due to the fabrication process and the penetrating silver electrode. The slope increases with increasing voltage, a varying slope could indicate a varying trap density which could be explained by the redistribution of silver ions. This process aligns with the ongoing formation of Ag filaments, which ultimately establish contact between both electrodes and establish the LRS. Meanwhile, the slope of LRS is 1, which is again in a good accordance with Ohmic conduction mechanism. The linear fit reveals that the device of HRS is dominated by SCLC mechanism, while LRS conforms to ohmic conduction. These findings suggest that a behavior similar to the formation of conducting filaments observed in thin-film memristors also occurs in our inkjet-printed HKUST-1 memristors. However, it remains uncertain whether the filaments grow along the grain boundaries or traverse the HKUST-1 structure, and this will be investigated in future studies.

A detailed benchmark of the presented memristor against other printed memory devices is presented in **Table 1**. In addition to the device structure, we have included details on the device type, device architecture, active layer fabrication temperature, forming voltage, set/reset voltage, R_{off}/R_{on} ratio, endurance, retention, scalability and power consumption. Device architectures are compared between cross-point (CP) and common-bottom (CB) memristor configurations, noting that CP devices enable integration into crossbar circuits, a feature not inherently supported by CB architectures. Power consumption of the memory device was calculated by the product of the switching voltage and current based on the *I–V* curve during the set process, and scalability was assessed using dimensions provided in the literature. The presented device demonstrates almost forming-free and a relatively higher R_{off}/R_{on} ratio. A key feature of our device is that the growth and formation of the HKUST-1 active layer occurs at room temperature, allowing for the use of a wide range of substrates in memristor fabrication. Although the current performance may not yet reach that of state-of-the-art devices, we believe that our memristor fabrication method can inspire further research. With continued optimization of the fabrication process, the memristor's performance can be significantly improved, opening up opportunities for future advancements.

3. Conclusion

In summary, we synthesized polycrystalline HKUST-1 films by combining inkjet printing technique and evaporation induced crystallization at room temperature. Furthermore, we developed an inkjet-printed memristor using HKUST-1 as active material. The memristor can be served as non-volatile memory with large R_{off}/R_{on} ratio of 10^4 for over 60 cycles and showed low forming voltages, potentially due to an increased ion diffusion caused by the porosity of HKUST-1. Moreover, we investigated the conduction mechanism of different resistive states of the memristor. The LRS is dominated by ohmic conduction whereas the behavior during HRS can be described by the SCLC theory. Filament formation and rupture through the HKUST-1 layer was postulated as switching mechanism. The reported memristor therefore was produced using additive manufacturing techniques and represents the first proof of principle that inkjet-printed MOFs are possible materials for memristors.

4. Experimental Section

Device Fabrication: *Treatment of ITO substrates*: Commercially available ITO substrates were laser patterned by Trumpf TruMicro 5000 ps laser, which was operated with an average power of 1.5 W. The dimensions of the patterned substrate were 30 µm.

Preparation of HKUST-1 Ink: 0.39 g $Cu(NO_3)_2 \cdot 2.5\ H_2O$ and 0.19 g 1,3,5-benzenetricarboxylic acid (BTC) were dissolved in 1.5 mL DMSO to form a transparent blue precursor solution. 1 mL of the HKUST-1 precursor solution was dispersed in a mixture of ethanol (2.3 mL) and ethylene glycol (1.5 mL) with vigorous stirring to obtain the homogeneous HKUST-1 ink, then the HKUST-1 ink was filtered by a 0.45 µm Nylon syringe filter, loaded into an empty cartridge and ready for printing.

Inkjet printing of HKUST-1 films and Ag electrodes: the HKUST-1 ink was inkjet-printed on the glass substrate with patterned ITO electrodes by a drop-on-demand piezo inkjet-printer (DMP2831, Fujifilm) at ≈40 V cartridge voltage. After the inkjet printing process, the printed substrate was immediately transferred into a desiccator containing methanol solution in a glass beaker for slow nucleation induced by methanol vapor. A membrane pump was then used to reduce the pressure to 30 mbar for 20 min. For printing additional layers, the mentioned steps were repeated. Afterward, the printed substrate was dried in vacuum overnight. Subsequently, the substrate was washed with methanol and dried with nitrogen gas. The thickness of the HKUST-1 layer could be controlled by repeating multiple printing cycles. A commercial Ag nanoparticle ink (Silverjet DGP, Sigma Aldrich) with a particle diameter of 10 nm was inkjet-printed on the top of HKUST-1 films at 33 V cartridge voltage with a drop spacing of 10 and annealed at 100 °C for 1 h.

Table 1. Performance comparison with other printed memory devices. CP: Cross-point, CB: Common-bottom electrode, -: Not or not clearly presented, n.a.: Not applicable, *: Estimated value reported in literature.

Device Structure	Device Type	Device Architecture	Active Layer Fabrication Temperature [°C]	Forming Voltage [V]	Set/Reset Voltage [V]	R_{off}/R_{on} Ratio	Endurance (Cycles)	Retention [s]	Power Consumption (SET) [µW]	Scalability [µm^2]	Refs.
Ag/WS_2/Ag	RS Memory	CP	120	–	2.3/−2.3	10^3	1.5×10^3	10^5	$\approx 10^3$	900	[50]
PEN/Al/PS:PCBM /Al/P3HT/Au/Al	1D-1R cell	CP	≈90	–	4/13	$\approx 10^3$	100	10^4	≈700	–	[51]
Ag/spin-on-glass(SOG) /PEDOT:PSS	RS Memory	CP	100–400	0.5	0.5/−0.05	10^4	10^3	1.6×10^4	≈0.5	$\approx 1.44 \times 10^4$	[52]
Ag/MEH: PPV-PMMA/Ag	RS Memory	CP	110	–	1.2/−1.2	10	50	4.2×10^5	1.2×10^5	$\approx 4 \times 10^4$	[53]
Ti/2D-InOx/Ti	RS Memory	CP	180	9	9/−9	10	100	6×10^3	1.8	–	[54]
Ag/TiO2/C	RS Memory	CB	50	1	1/−2.5	983.9	100	3×10^4	≈100	$\approx 7 \times 10^4$	[55]
Ag/GQD–hBN/Ag	RS Memory	CP	120	≈8	4/−4	$>10^3$	10^3	10^5	4×10^3	–	[56]
Ag/ZnO/Ag	RS Memory	CP	400	1.5	1.52/0.38	10^7	100	$\geq 10^4$	$\approx 1.2 \times 10^3$	2.25×10^4	[57]
ITO/hBN-MoS2 QDs/Ag	RS Memory	CB	120	≈2.5	1.4/1	$>10^3$	10^3	10^4	140	1.385×10^3	[58]
Ag/P(VDF-TrFE)/DTBDT-C6/PS	Charge Trapping Transistor	n.a.	100	n.a.	−25/30	$>10^3$	10	>10 years*	–	–	[59]
Au/P(NDI2OD-T2)/PMMA-Au	Floating Gate Transistor	n.a.	80	n.a.	−80/80	$\approx 10^5$	100	$>10^7$	–	–	[60]
ITO/HKUST-1/Ag	RS Memory	CP	RT	~1	1.45/−0.80	10^4	60	600	500	$\approx 4.5 \times 10^3$	This work

Material Characterization: X-ray diffraction patterns were recorded on a Bruker D8 Discover diffractometer in Bragg Brentano geometry with Ni-filtered Cu -Kα (λ = 1.54060 Å) radiation source in theta/2theta mode, with a step width of 0.02°. AFM was performed using a Bruker Dimension Icon Atomic Force Microscope in tapping mode equipped with a silicon cantilever (HQ:NSC15/AL BS, MikroMasch) for morphology characterization. FTIR spectra were recorded with a Nicolet Is50 FTIR from Thermo Fisher Scientific in ATR mode. The scan range was 400–4000 cm^{-1}. SEM was performed on a Thermo Fischer ESEM Quattro S. FIB preparation were performed using a JEOL Focused Ion Beam System JEM-9320FIB. The surface tension of the HKUST-1 ink was measured by pendant drop method using Krüss DSA100. The viscosity of the HKUST-1 ink was measured using a rotational rheometer from Haake Mars. The contact angle was measured using the OCA-20 system from DataPhysics Instruments GmbH, following the sessile drop method.

Electrical Characterization: *Sweeping Switch Measurement*: For the positive sweeping process, the bias voltage was swept from 0 V to a positive voltage and then back to 0 V, while the negative sweep process was the opposite, sweeping from 0 V to a negative voltage and then back to 0V. During the sweeping process, the device switching between HRS and LRS was performed using a CC to protect the device from damaging by an excessive current.

Resistance Read-Out Pulse: Resistance is measured after each sweeping process, in order to avoid the resistance state of devices being changed, a pulse voltage of 0.01 V for 0.2 s was applied to obtain the value of resistance.

Retention Measurement: The retention measurement was performed after the memristor was switched to LRS or HRS, to investigate the resistance change after device switching. In this work, the resistance was read out by a pulse voltage of 0.01 V for 0.2 s after the device was switched to a resistant state, then repeated every 6s for 100 times.

Supporting Information

Supporting Information is available from the Wiley Online Library or from the author.

Acknowledgements

Y.L., H.H., and J.A.-H. acknowledge funding by the DFG under Germany's Excellence Strategy via the Excellence Cluster "3D Matter Made to Order" (EXC-2082/1-390761711). B.B. and J.A.-H. acknowledge financial support from the KIT via the project Auto.MAP and the Helmholtz Program "Materials Systems Engineering" under program no. 43.31.01.

Open access funding enabled and organized by Projekt DEAL.

Conflict of Interest

The authors declare no conflict of interest.

Data Availability Statement

The data that support the findings of this study are available from the corresponding author upon reasonable request.

Keywords

HKUST-1, inkjet printing, memristor, metal–organic framework

Received: July 12, 2024
Revised: November 29, 2024
Published online: December 16, 2024

[1] S. R. Forrest, *Nature* **2004**, *428*, 911.
[2] B.-J. de Gans, P. C. Duineveld, U. S. Schubert, *Adv. Mater.* **2004**, *16*, 203.
[3] K. Yan, J. Li, L. Pan, Y. Shi, *APL Mater.* **2020**, *8*, 120705.
[4] H. D. Goldberg, R. B. Brown, D. P. Liu, M. E. Meyerhoff, *Sens. Actuators, B* **1994**, *21*, 171.
[5] Q. Huang, Y. Zhu, *Sci. Rep.* **2018**, *8*, 15167.
[6] P. M. Harrey, B. J. Ramsey, P. S. A. Evans, D. J. Harrison, *Sens. Actuators, B* **2002**, *87*, 226.
[7] J. Xie, J. Jiang, P. Davoodi, M. P. Srinivasan, C.-H. Wang, *Chem. Eng. Sci.* **2015**, *125*, 32.
[8] S. Kim, H. Sojoudi, H. Zhao, D. Mariappan, G. H. McKinley, K. K. Gleason, A. J. Hart, *Sci. Adv.* **2016**, *2*, e1601660.
[9] M. Singh, H. M. Haverinen, P. Dhagat, G. E. Jabbour, *Adv. Mater.* **2010**, *22*, 673.
[10] P. Calvert, *Chem. Mater.* **2001**, *13*, 3299.
[11] H. Li, M. Eddaoudi, M. O'Keeffe, O. M. Yaghi, *Nature* **1999**, *402*, 276.
[12] H.-C. Zhou, J. R. Long, O. M. Yaghi, *Chem. Rev.* **2012**, *112*, 673.
[13] D. Alezi, Y. Belmabkhout, M. Suyetin, P. M. Bhatt, Ł. J. Weseliński, V. Solovyeva, K. Adil, I. Spanopoulos, P. N. Trikalitis, A.-H. Emwas, M. Eddaoudi, *J. Am. Chem. Soc.* **2015**, *137*, 13308.
[14] H. Daglar, H. C. Gulbalkan, G. Avci, G. O. Aksu, O. F. Altundal, C. Altintas, I. Erucar, S. Keskin, *Angew. Chem., Int. Ed.* **2021**, *60*, 7828.
[15] X. Yang, S. Yuan, L. Zou, H. Drake, Y. Zhang, J. Qin, A. Alsalme, H.-C. Zhou, *Angew. Chem., Int. Ed.* **2018**, *57*, 3927.
[16] L. Feng, S. Yuan, J.-L. Li, K.-Y. Wang, G. S. Day, P. Zhang, Y. Wang, H.-C. Zhou, *ACS Cent. Sci.* **2018**, *4*, 1719.
[17] S. Kim, J. Lee, S. Jeoung, H. R. Moon, M. Kim, *Chem. – Eur. J.* **2020**, *26*, 7568.
[18] M.-S. Yao, J.-W. Xiu, Q.-Q. Huang, W.-H. Li, W.-W. Wu, A.-Q. Wu, L.-A. Cao, W.-H. Deng, G.-E. Wang, G. Xu, *Angew. Chem., Int. Ed.* **2019**, *58*, 14915.
[19] M. Meilikhov, S. Furukawa, K. Hirai, R. A. Fischer, S. Kitagawa, *Angew. Chem., Int. Ed.* **2013**, *52*, 341.
[20] Y. Peng, J. Xu, J. Xu, J. Ma, Y. Bai, S. Cao, S. Zhang, H. Pang, *Adv. Colloid Interface Sci.* **2022**, *307*, 102732.
[21] G. Ding, Y. Wang, G. Zhang, K. Zhou, K. Zeng, Z. Li, Y. Zhou, C. Zhang, X. Chen, S.-T. Han, *Adv. Funct. Mater.* **2019**, *29*, 1806637.
[22] G. Lu, O. K. Farha, W. Zhang, F. Huo, J. T. Hupp, *Adv. Mater.* **2012**, *24*, 3970.
[23] A. Razmjou, M. Asadnia, O. Ghaebi, H.-C. Yang, M. E. Warkiani, J. Hou, V. Chen, *ACS Appl. Mater. Interfaces* **2017**, *9*, 38076.
[24] T. Ladnorg, A. Welle, S. Heißler, C. Wöll, H. Gliemann, *Beilstein J. Nanotechnol.* **2013**, *4*, 638.
[25] H. K. Arslan, O. Shekhah, J. Wohlgemuth, M. Franzreb, R. A. Fischer, C. Wöll, *Adv. Funct. Mater.* **2011**, *21*, 4228.
[26] S. Eslava, L. Zhang, S. Esconjauregui, J. Yang, K. Vanstreels, M. R. Baklanov, E. Saiz, *Chem. Mater.* **2013**, *25*, 27.
[27] J.-L. Zhuang, D. Ar, X.-J. Yu, J.-X. Liu, A. Terfort, *Adv. Mater.* **2013**, *25*, 4631.
[28] P. Goel, S. Singh, H. Kaur, S. Mishra, A. Deep, *Sens. Actuators, B* **2021**, *329*, 129157.
[29] J.-L. Zhuang, D. Ceglarek, S. Pethuraj, A. Terfort, *Adv. Funct. Mater.* **2011**, *21*, 1442.
[30] R. Tetzlaff, *Memristors and Memristive Systems*, Springer, New York, New York, NY **2014**.
[31] M. Lanza, A. Sebastian, W. D. Lu, M. L.e Gallo, M.-F. Chang, D. Akinwande, F. M. Puglisi, H. N. Alshareef, M. Liu, J. B. Roldan, *Science* **2022**, *376*, eabj9979.
[32] Y. Pang, B. Gao, B. Lin, H. Qian, H. Wu, *Adv. Electron. Mater.* **2019**, *5*, 1800872.
[33] R. Dittmann, S. Menzel, R. Waser, *Adv. Phys.* **2021**, *70*, 155.
[34] A. Sajedi-Moghaddam, E. Rahmanian, N. Naseri, *ACS Appl. Mater. Interfaces* **2020**, *12*, 34487.

[35] A. Sajedi-Moghaddam, M. Gholami, N. Naseri, *ACS Appl. Mater. Interfaces* **2023**, *15*, 3894.
[36] B. Derby, *Annu. Rev. Mater. Res.* **2010**, *40*, 395.
[37] N. Afsahi, M. Majumder, N. Naseri, *Chem. Eng. J.* **2024**, *493*, 152356.
[38] D. Nečas, P. Klapetek, *Eur. J. Phys.* **2012**, *10*, 181.
[39] R. Waser, R. Dittmann, G. Staikov, K. Szot, *Adv. Mater.* **2009**, *21*, 2632.
[40] I. Valov, M. N. Kozicki, *J. Phys. D: Appl. Phys.* **2013**, *46*, 074005.
[41] W. Sun, B. Gao, M. Chi, Q. Xia, J. J. Yang, H. Qian, H. Wu, *Nat. Commun.* **2019**, *10*, 3453.
[42] Y. Yang, P. Gao, S. Gaba, T. Chang, X. Pan, W. Lu, *Nat. Commun.* **2012**, *3*, 732.
[43] R. Waser, M. Aono, *Nat. Mater.* **2007**, *6*, 833.
[44] Y. Liu, H. Wang, W. Shi, W. Zhang, J. Yu, B. K. Chandran, C. Cui, B. Zhu, Z. Liu, B. Li, C. Xu, Z. Xu, S. Li, W. Huang, F. Huo, X. Chen, *Angew. Chem., Int. Ed.* **2016**, *55*, 8884.
[45] T. Nhu Hoang Tran, T. Hoang Le, H. Kieu Thi Ta, Y. Thi Dang, L. Thuy Ho Nguyen, T. Hoang Le Doan, C.-K. Fang, I.-S. Hwang, T. Bach Phan, N. K. Pham, *Org. Electron.* **2021**, *93*, 106136.
[46] R. Waser, R. Dittmann, G. Staikov, K. Szot, *Adv. Mater.* **2009**, *21*, 2632.
[47] J. Zhu, T. Zhang, Y. Yang, R. Huang, *Appl. Phys. Rev.* **2020**, *7*, 11312.
[48] G. Ding, Y. Wang, G. Zhang, K. Zhou, K. Zeng, Z. Li, Y. Zhou, C. Zhang, X. Chen, S.-T. Han, *Adv. Funct. Mater.* **2019**, *29*, 1806637.
[49] L. Liu, J. Dong, J. Liu, Q. Liang, Y. Song, W. Li, S. Lei, W. Hu, *Small Struct.* **2021**, *2*, 2000077.
[50] M. M. Rehman, G. U. Siddiqui, Y. H. Doh, K. H. Choi, *Semicond. Sci. Technol.* **2017**, *32*, 095001.
[51] Y. Ji, D. F. Zeigler, D. S. Lee, H. Choi, A. K.-Y. Jen, H. C. Ko, T.-W. Kim, *Nat. Commun.* **2013**, *4*, 2707.
[52] B. Huber, P. B. Popp, M. Kaiser, A. Ruediger, C. Schindler, *Appl. Phys. Lett.* **2017**, *110*, 143503.
[53] M. M. Rehman, B.-S. Yang, Y.-J. Yang, K. S. Karimov, K. H. Choi, *Curr. Appl Phys.* **2017**, *17*, 533.
[54] C.-H. Huang, C.-Y. Weng, K.-H. Chen, Y. Chou, T.-L. Wu, Y.-C. Chou, *ACS Appl. Mater. Interfaces* **2023**, *15*, 25838.
[55] D.-H. Lien, Z.-K. Kao, T.-H. Huang, Y.-C. Liao, S.-C. Lee, J.-H. He, *ACS Nano* **2014**, *8*, 7613.
[56] M. M. Rehman, G. U. Siddiqui, S. Kim, K. H. Choi, *J. Phys. D: Appl. Phys.* **2017**, *50*, 335104.
[57] H. Hu, A. Scholz, Y. Liu, Y. Tang, G. C. Marques, J. Aghassi-Hagmann, *IEEE Trans. Electron Devices* **2023**, *70*, 3051.
[58] M. M. Rehman, G. U. Siddiqui, M. M. ur Rehman, H. B. Kim, Y. H. Doh, K. H. Choi, *Mater. Res. Bull.* **2018**, *105*, 28.
[59] W. Kim, J. Kwon, Y. Takeda, T. Sekine, S. Tokito, S. Jung, *Adv. Mater. Technol.* **2021**, *6*, 2100141.
[60] M. Kang, K.-J. Baeg, D. Khim, Y.-Y. Noh, D.-Y. Kim, *Adv. Funct. Mater.* **2013**, *23*, 3503.